International Journal of Solids and Structures 162 (2019) 87–95

Contents lists available at ScienceDirect

International Journal of Solids and Structures

journal homepage: www.elsevier.com/locate/ijsolstr

Limiting strain for auxeticity under large compressive deformation: Chiral vs. re-entrant cellular solids

Yunyao Jiang[a], Bodhi Rudra[b], Jongmin Shim[b,*], Yaning Li[a,*]

[a] Department of Mechanical Engineering, University of New Hampshire, United States of America
[b] Department of Civil, Structural and Environmental Engineering, University at Buffalo, United States of America

ARTICLE INFO

Article history:
Received 20 May 2018
Revised 27 November 2018
Available online 1 December 2018

Keywords:
Auxetic
Re-entrant
Chiral
3D-printing
Cellular solids
Mechanical metamaterial

ABSTRACT

Under compression, auxetic open cell cellular solids may lose auxeticity due to instability and/or self-contact between the ribs. This study explores the limiting strains for preserving auxetic effects for auxetic open cell materials of two different cellular structures: re-entrant honeycomb and the 'missing-rib' type chiral cellular solids. Experiments of the 3D printed specimens, periodicity analysis, and ellipticity analysis showed that, under compressive loads, the auxetic effects and the limiting compressive strain for auxeticity are mutually exclusive. In other words, the limiting compressive strain has to be reduced if larger auxetic effect is desired, *vice versa*. It was found that compared with re-entrant honeycombs, due to chirality-induced rotation, the chiral cellular solids can preserve auxetic effects under much larger compressive strain (>−10–30%).

© 2018 Elsevier Ltd. All rights reserved.

1. Introduction

The auxetic open-cell cellular solids have broad engineering applications (Lakes, 1987; Lakes and Elms, 1993; Chan and Evans, 1998; Evans and Alderson, 2000; Chen and Lakes, 1989; Scarpa et al., 2003) due to the light weight, auxetic effects (Dolla et al., 2007; Arruebo, 2012; Fozdar et al., 2011; Wu et al., 2015; Smith, 1991; Guiducci et al., 2014), and superior acoustic properties (Chen and Lakes, 1989; Scarpa et al., 2003; Bertoldi et al., 2010; Tee et al., 2010; Shim et al., 2013; Wang et al., 2014a; Tang et al., 2015). As one of the earliest auxetic open-cell materials, re-entrant honeycomb was developed from hexagonal honeycomb by introducing re-entrant angles (Lakes, 1987), as shown in Fig. 1a. The major mechanism for auxeticity is that the ribs forming the re-entrant angle rotate in/out upon uni-axial compression/tension.

In 1990 s, as another category of auxetic open cell materials, chiral cellular solids were proposed (Lakes and Elms, 1993), such as a triangular lattice with central rings (Prall and Lakes, 1997), and a 'missing-rib' honeycomb which was created by selectively deleting some of the ribs in a diamond honeycomb (Smith et al., 2000), as shown in Fig. 1b. For both category of auxetic open cell materials, the auxetic effect is induced by the rotation of slant ribs. As shown in Fig. 1, the slant ribs in a re-entrant cell rotate in opposite directions due to the mirror symmetry of the structure, but the ribs in a chiral cell rotate in the same direction. Therefore, cells with chiral geometry have deterministic handedness and are expected to have more robust Poisson's ratio performance (Sigmund and Torquato, 1997; Wang et al., 2014b; Grima et al., 2016). In previous work (Jiang and Li, 2017a), the relationship between the internal rotation and the auxetic effects of the 'missing-rib' type of chiral cellular solids was extensively quantified, and it was concluded that the auxetic effect can be amplified by elevating the internal rotation. By utilizing the concept of chirality-induced auxeticity, new chiral auxetic open cell cellular solids were designed with new sequential cell opening mechanisms (Jiang and Li, 2017b and 2018).

There is another active avenue of research on instability-induced auxetic effects in porous materials and lattice structures (Babaee et al., 2013; Bertoldi and Boyce, 2008; Shim et al., 2013; Wang et al., 2014c; Zhang et al., 2015; Haghpanah et al., 2014). It provided an interesting concept of designing instability-induced auxetic materials. After instability, initial symmetric structures lose its symmetry, leading to auxetic effects. However, the deformed shape of the symmetric auxetic structures is not deterministic because the handedness of the first buckled unit cell is randomly selected and determines the overall buckled shape. In contrast, the chiral auxetic open cell materials have deterministic chirality, and the mechanical behavior and properties of them can be well-controlled by the geometry and material composition.

In this study, mechanical experiments on 3D printed prototypes of the re-entrant honeycomb and the 'missing-rib' type chiral cells were performed under uni-axial compression. The nonlinear mechanical behaviors of both designs under large compressive loads

---

* Corresponding authors.
E-mail addresses: jshim@buffalo.edu (J. Shim), yaning.li@unh.edu (Y. Li).

https://doi.org/10.1016/j.ijsolstr.2018.11.035
0020-7683/© 2018 Elsevier Ltd. All rights reserved.

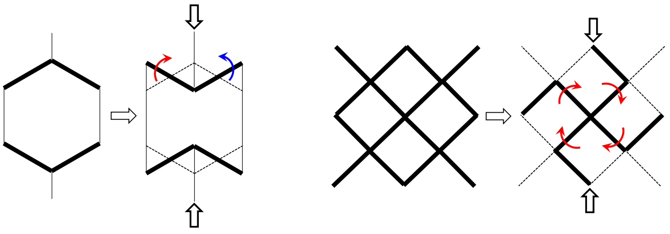

Fig. 1. (a) The mechanism of re-entrant angle induced auxeticity and (b) the mechanism of chirality induced auxeticity.

were investigated via both mechanical experiments and finite element simulations. Through numerical stability analysis of both designs with the consideration of geometric constrains, we calculated the limiting strain for preserving auxetic effects for each of the two different cellular configurations.

2. The designs of the re-entrant and chiral specimens

Specimens of a re-entrant honeycomb and a missing-rib type of chiral cellular solids were designed in CAD software Solidworks. The representative volume element (RVE) of each specimen is shown in Fig. 2a. For the re-entrant honeycomb, the cell geometry is determined by two non-dimensional parameters, the ratio between vertical segment and slant segment h/l and the re-entrant angle θ (θ is negative), as shown in Fig. 2a (left). For the chiral specimen, the geometry is determined by the corner angles α and β, and the rib length a, (see Fig. 2a (right)). The ribs in the chiral specimen have the same length.

The 3D geometries of the two specimens are shown in Fig. 2b. The geometric parameters for the reentrant honeycomb were chosen as $h/l = 2$ ($h = 11.55$ mm and $l = 5.77$ mm) and $\theta = 30°$; and those of the chiral specimen were chosen as $a = 3.54$ mm, $\alpha = \beta = 90°$. The overall dimensions for both specimens are 50 mm × 50 mm × 20 mm along directions 1, 2, and 3, respectively. In order to keep the material volume fraction of the two specimens the same (~38%), the two specimens possess the slightly different in-plane thicknesses of the ribs. As shown in Fig. 2b, for the re-entrant honeycomb, the in-plane thickness of the ribs $t_h = 1.59$ mm, and for the chiral specimen, the in-plane thickness of the ribs t_c=1.50 mm.

3. Mechanical experiments on the 3D-printed specimens

The two designs were then fabricated via a multi-material 3D printer (Objet Connex 260), and a digital material DM9760 (with shear modulus ~0.92 MPa) from the 3D printer was used as the model material for both specimens. To allow fully curing, the printed specimens were kept under room temperature for 24 h before mechanical experiments. The specimens were then placed between two compression disks which are mounted on a Zwick/Roell material testing machine. Mechanical experiments under quasi-static uniaxial compression were performed. The overall strain rate was controlled as 10^{-3} per second. To track the deformation of the specimens, dark markers were added on the specimens (Fig. 3c), and a high resolution camera was used to track the displacement of each marker during the experiments.

For the re-entrant honeycomb, uniaxial compression experiments were performed along in directions 1 and 2, respectively. While for the chiral one, the experiments were only performed in direction 2 because the properties along directions 1 and 2 are the same due to the four-fold symmetry of the chiral specimen.

Finite element simulations of the experiments on the two designs were performed in ABAQUS/STANDARD V6.13. Four-node 2D plane stress elements (CPS4) were used. In the FE models, two types of boundary conditions were applied: one is that the bottom edge is fixed in both horizontal and vertical directions, and a prescribed displacement in vertical direction was applied at the top edge to represent the uni-axial compression (the solid lines in Fig. 3a), which is to model the boundary conditions in the mechanical experiment; and the other is periodic boundary condition (the dash lines in Fig. 3b), which is to represent the case with infinite numbers of cells.

In all FE models, the nonlinear geometry effect was considered and contact between the ribs were defined. For the model ma-

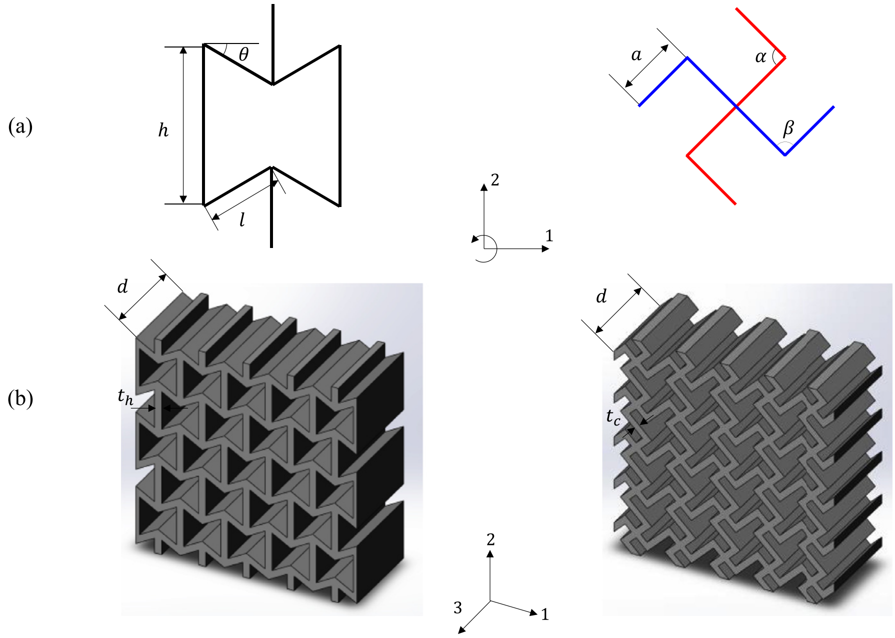

Fig. 2. (a) The schematic drawings of the representative volume element (RVE) of the re-entrant honeycomb (left) specimen and the chiral specimen (right), and (b) the 3D geometry of the two specimens.

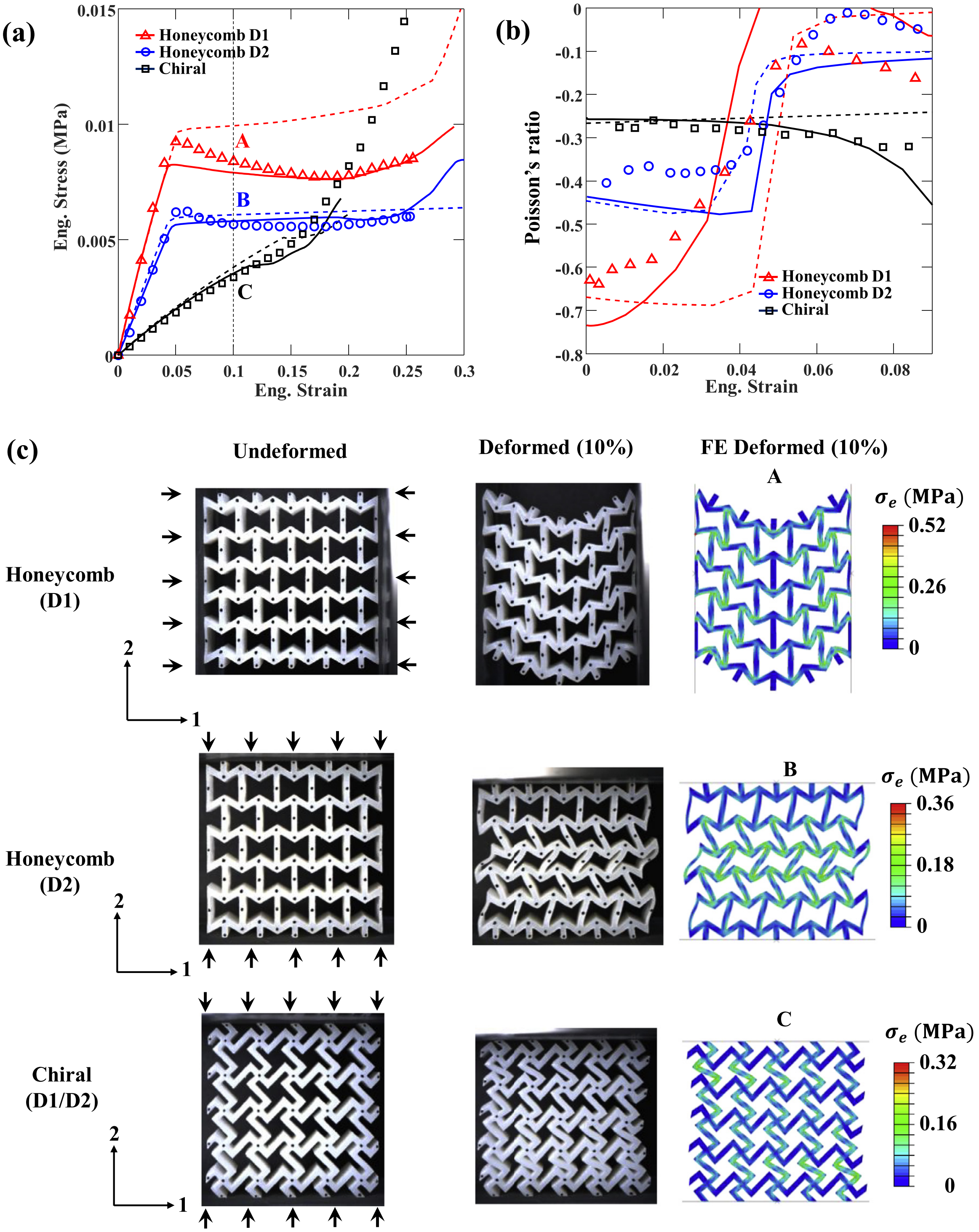

Fig. 3. (a) Engineering stress vs. engineering strain (left) and the Poisson's ratio vs. overall engineering strain curve (right) (Symbols are experimental data; the solid lines are FE results with experimental boundary conditions; and the dash lines are FE results with periodic boundary conditions). (b) The undeformed and deformed configurations of the re-entrant honeycomb compressed in direction 1 (A), in direction 2 (B), and those of the chiral specimen (C).

terial DM9760, incompressible hyperelastic Mooney-Rivlin model was used. The strain energy density function W of the Mooney-Rivlin model is $W = C_{10}(I_1 - 3) + C_{01}(I_2 - 3)$, where I_1 and I_2 are the first and second invariants of left Cauchy-Green deformation tensor. The material parameters, C_{10} and C_{01}, were obtained from the standard experiments of both uni-axial tension and compression of the material: C_{01}=0.46 MPa, C_{10}=0 MPa, (in the true strain range of ~ -0.8–0.4). These material parameters were then input into ABAQUS for FE simulations. The results from experiments and FE simulations with the two different boundary conditions are shown in Fig. 3.

The mechanical response of the two specimens are quite different. For the re-entrant honeycomb shown in Fig. 3a, the curves in both directions show a linear increase up to ∼3–4% strain followed by a plateau with slight softening. Then hardening occurs when the overall strain goes beyond ~25%. In the initial linear range, the stiffness and the peak stress of the re-entrant honeycomb compressed in direction 1 is higher than that in direction 2, but the overall strains at the peaks and the incipient of strain at the hardening in the two directions are almost identical.

For the chiral specimen, as shown in Fig. 3a, the stress increases monotonically with the strain, and no peak/sharp turning points were observed in the stress-strain curves. The curve increases almost linearly at the beginning and hardens after ~16% overall strain. Hardening occurs earlier and much more dramatic for the chiral specimen than the re-entrant honeycomb. The FE results with the experimental boundary conditions (solid lines) show that the hardening part of the stress-strain curves are indebted to the densification of the specimen and the contact between the ribs under large deformation. On the other hand, the FE results with periodic boundary conditions are generally higher than those of experiments. For the re-entrant honeycomb specimen compressed in direction 1, the FE results with periodic boundary conditions are much higher than the experimental data, indicating the results are sensitive to the numbers of cells in the specimen. For the re-entrant honeycomb specimen compressed in direction 2 (D2) and the chiral specimen, the FE results with periodic boundary conditions are only slightly higher than the experimental data. The effects of numbers of cells on the instability will be further explored in Section 4.

As shown in Fig. 3b, for the re-entrant honeycomb, the initial Poisson's ratio is ~ -0.6 in direction 1 and ~ -0.4 in direction 2. When the over strain reaches ~3 and 4% which is coincident with the peaks of the stress-strain curves, the Poisson's ratios in both directions increase dramatically. This indicates that the peak stress in the stress-strain curves is relating to the instability, after which the auxetic effects are lost in both directions. On the other hand, the Poisson's ratio of the chiral specimen keeps as a constant ~ -0.3 before hardening.

The undeformed and deformed (at 10% overall strain) configurations of the two specimens are shown in Fig. 3c. When the re-entrant honeycomb is subject to compression in direction 1, instability occurs with the entire specimen bulged out to one side. For the re-entrant honeycomb compressed in direction 2, localized instability occurs within two middle horizontal layers of cells. However, the deformation within the chiral specimen is quite uniform, and there is no dramatic change in cell patterns during the deformation.

For re-entrant honeycomb structures subjected to compression, these results show that instability occurs under relatively small deformation (~3 and 4%) and the auxetic effect diminishes after instability. On the other hand, the chiral specimen preserves the auxetic effects under much larger deformation. Under large deformation, the constant auxetic effects and the significant volume reduction of the chiral structure lead to more dramatic and earlier hardening of the chiral specimen than those of the re-entrant honeycomb.

4. Numerical results for the instability of re-entrant honeycomb

Generally, there are two possible types of instability for periodic cellular solids. Upon application of deformation, an infinitely periodic structure can change its periodicity due to mechanical instability, which could be either microscopic (i.e., with wavelengths that are of the order of the size of the microstructure) or macroscopic (i.e., with much larger wavelengths than the size of the microstructure) (Triantafyllidis and Maker, 1985; Waas et al., 1990; Geymonat et al., 1993; Ji and Waas, 2007; Bertoldi and Boyce, 2008). In fact, generally, whether the microscopic/macroscopic instability will occur or there is no instability depend on the material properties and cell geometry.

Table 1
The geometric parameters of nine FE models.

Model no.	h (mm)	l (mm)	t (mm)	θ	h/l	l/t	ρ
A1	11.55	5.77	2.20	10°	2	2.62	0.38
A2	11.55	5.77	1.59	30°	2	3.63	0.38
A3	11.55	5.77	1.11	45°	2	5.20	0.38
A4	8.66	5.77	1.83	10°	1.5	3.15	0.38
A5	8.66	5.77	1.20	30°	1.5	4.81	0.38
A6	8.66	5.77	0.90	40°	1.5	6.41	0.38
A7	5.77	5.77	1.48	5°	1	3.90	0.39
A8	5.77	5.77	1.33	10°	1	4.35	0.39
A9	5.77	5.77	0.9833	20°	1	5.92	0.38

In the present investigation, both instability analyses of the two basic auxetic cellular solids are performed. The detailed numerical procedure to investigate the instability of periodic structures are presented in the Appendix **S1** (micro-instability) and **S2** (macro-instability). FE models of unit cells of both cellular solids with various geometries were developed in ABAQUS/CAE. Four-node 2D plane stress elements (CPS4) were used. To determine the critical strain and mode for instability for the re-entrant honeycombs, we performed FE simulations by using a unit-cell model with periodic boundary conditions for microscopic and macroscopic instability analyses in both directions 1 and 2.

The periodic boundary conditions are introduced at all four edges of the unit cell by prescribing displacement $\mathbf{u}$ where $\mathbf{u}_\beta = \mathbf{u}_\alpha + (\bar{\mathbf{F}}^{\mathrm{app}} - \mathbf{1})(\mathbf{X}_\beta - \mathbf{X}_\alpha)$, in which the subscripts α and β indicate two nodal points periodically located at unit-cell boundaries, $\mathbf{1}$ represents the second order identity tensor, and $\bar{\mathbf{F}}^{\mathrm{app}}$ represents the macroscopic deformation gradient imposed on two positions $\mathbf{X}_\alpha$ and $\mathbf{X}_\beta$. Virtual nodes are utilized to prescribe the macroscopic deformation gradient $\bar{\mathbf{F}}^{\mathrm{app}}$ at their degrees of freedom. The FE results are presented in this section.

4.1. Instability of re-entrant honeycomb in direction 1

To investigate the influences of geometry on the instability of the re-entrant honeycomb, finite element models of nine different RVEs were developed in ABAQUS by varying the two non-dimensional geometric parameters h/l and θ while keeping l as 5.77 mm, as shown in **Table 1**. To keep the overall volume density as ~38%, the rib thickness of each model varies.

The unit-cell of Model A2 employed in FE simulation is shown in Fig. 4a. The results of microscopic instability (i.e., periodicity analysis, Appendix **S1**) are presented in Fig. 4b, where the evolution of the first natural frequency of various periodicities (indicated as the legends in Fig. 4b.) are monitored as compressive strain increases. Note that the periodicity shown as the legend in Fig. 4b is denoted by (N_v, N_d) or $N_v \times N_d$, where N_v and N_d are the numbers of unit cells in the first lattice direction (i.e., direction a, as shown in Fig. 4a) and the second lattice direction (i.e., direction b, as shown in Fig. 4a), respectively. Fig. 4b shows that the microscopic instability analysis suggests that $(1,\ N_d)$-periodicity becomes critical (i.e., when the minimum strain corresponding to the zero first natural frequency is reached) as N_d increases. Fig. 4c further confirms that the behavior of the microscopic instability (i.e., $\lim_{N_d \to \infty} (1, N_d)$) converges to that of the macroscopic instability (i.e., ellipticity analysis, Appendix **S2**).

The same numerical procedure is adopted for eight other geometries and their results are summarized in **Table 2**.

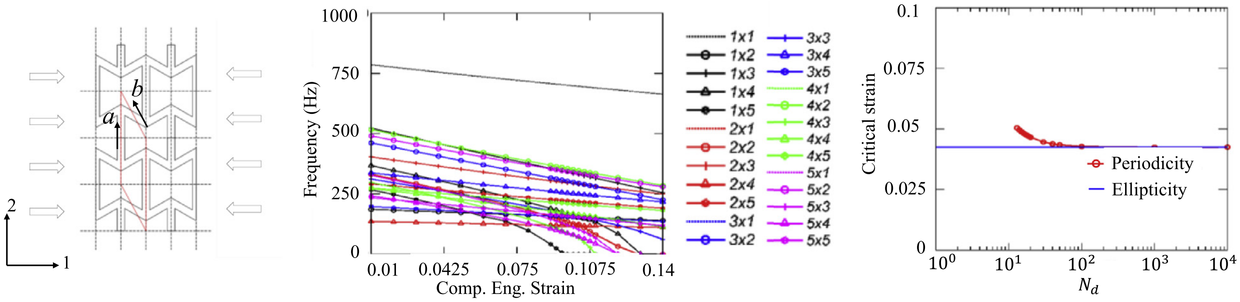

(a) (b) (c)

Fig. 4. (a) Schematic figure showing unit cell for re-entrant honeycomb (Model A2) compressed in direction 1 (D1), (b) microscopic instability analysis for Model A2 showing smallest eigenfrequency versus applied compressive strain, and (c) the effect of N_d in the periodicity (1, N_d) of the Model A2. The microscopic instability (periodicity analysis) converges to macroscopic instability (ellipticity analysis) results.

Table 2
Geometry and instability analysis results from re-entrant honeycomb compressed in direction D1.

Model no.	A1	A2	A3	A4	A5	A6	A7	A8	A9
Critical mechanism	Macroscopic instability at (1,∞)	(1, ∞)	(1, ∞)	(1, ∞)	(1, ∞)	(1, ∞)	(1, ∞)	(1, ∞)	(1, ∞)
Critical strain	.035	.0425	.07	.03	.0425	.0575	.025	.02	.0275

Table 3
Instability analysis results from re-entrant honeycomb compressed in direction 2 ($h = 11.55$ mm, $l = 5.77$ mm, and $\theta = 30°$).

Model no.	B1	B2	B3(=A2)	B4	B5	B6
t (mm)	2.00	1.75	1.59	1.50	1.25	1.00
Critical mechanism	Microscopic instability at (1, 2)	Microscopic instability at (1, 2)	Microscopic instability at (1, 2)	Microscopic instability at (1, 2)	Microscopic instability at (1, 2)	Microscopic instability at (1, 2)
Critical strain	0.055	0.0475	0.045	0.0425	0.0375	0.035

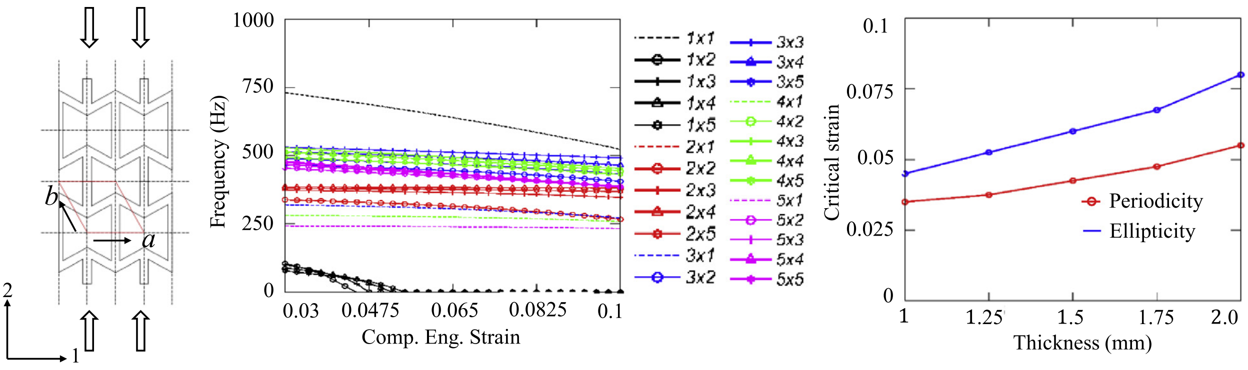

(a) (b) (c)

Fig. 5. (a) Schematic figure showing unit cell for re-entrant honeycomb compressed in direction 2, (b) microscopic instability analysis for model B3 showing smallest eigenfrequency versus applied compressive strain, and (c) the effect of thickness in the critical strain relating to instability.

4.2. Instability of re-entrant honeycomb in direction 2

For the re-entrant honeycomb, h, l, θ are kept the same as those in the experiment ($h = 11.55$ mm, $l = 5.77$ mm, and $\theta = 30°$), while the rib thickness varies as 2.0 mm, 1.75 mm, 1.59 mm, 1.50 mm, 1.25 mm, and 1.0 mm. FE simulations with total six different rib thicknesses were performed. The FE model dimensions and results are summarized in **Table 3**.

The geometry of Model B3 shown in Fig. 5a is the same as Model A2 and that of the 3D printed specimen. Note that the periodicity of the re-entrant honeycomb in direction 2 is denoted by (N_h, N_d) or $N_h \times N_d$, where N_h and N_d are number of units in the first lattice direction (i.e., direction a, as shown in Fig. 5a) and the second lattice direction (i.e., direction b, as shown in Fig. 5a), respectively. By taking model B3 as an example, the numerical results of microscopic and macroscopic instability of in direction 2 are shown in Fig. 5b and c.

Table 4
Geometry and instability analysis results for the chiral structure.

Model no.	t (mm)	α (degrees)	β (degreed)	a(mm)	Critical mechanism	Critical strain
C1	1.0	90°	90°	$\frac{5\sqrt{2}}{2}$	Macroscopic instability at $(1, \infty)$	.085
C2	1.5	90°	90°	$\frac{5\sqrt{2}}{2}$	Macroscopic instability at $(1, \infty)$	.085

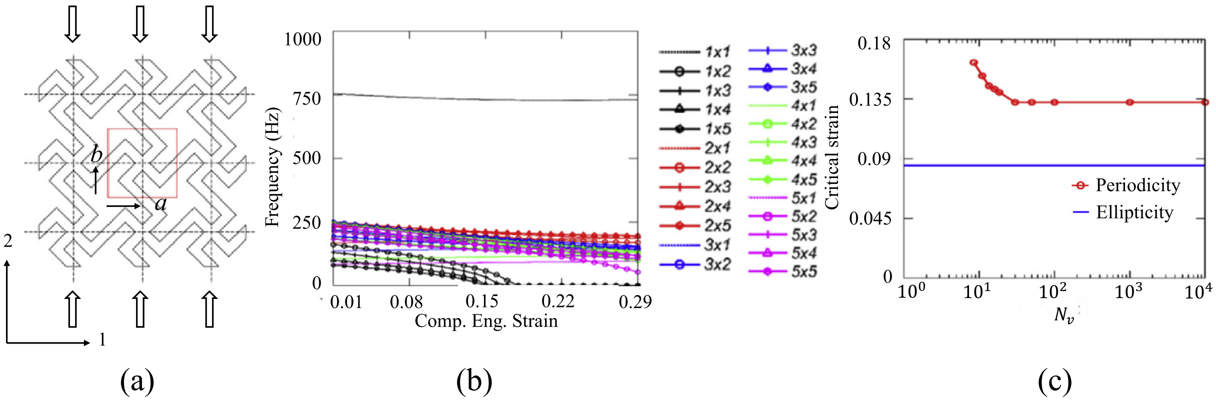

Fig. 6. (a) Schematic figure showing the unit cell of chiral structure, (b) microscopic instability analysis for Model C2 showing smallest eigenfrequency versus applied compressive strain, and (c) the effect of N_v in the periodicity $(1,\ N_v)$ of the Model C2.

Fig. 5b shows that the critical periodicity, which is the minimum number of unit cells for the lowest overall instability strain corresponding to microscopic instability, is (1, 2); and Fig. 5c confirms that the critical instability for model B3 is microscopic because the critical strain from macroscopic instability (ellipticity analysis) is greater than that from microscopic instability. In addition, the periodic pattern of (1, 2) periodicity is consistent with the pattern observed in the experiment. This procedure is adopted for five other geometries and their results are summarized in **Table 3**.

According to the instability analysis in this section, the re-entrant honeycomb structures under direction-2 compression will be dictated by microscopic instability.

4.3. Instability of chiral cell

In order to investigate the instability of the chiral structure, we consider chiral cell with two different rib thickness. The dimensions are summarized in **Table 4.**

A schematic pattern and the FE model of a unit-cell are shown in Fig. 6a for the geometry of Model C2. Note that the periodicity of the re-entrant honeycomb in direction 2 is denoted by (N_h, N_v) or $N_h \times N_v$, where N_h and N_v are number of units in the first lattice direction (i.e., direction a, as shown in Fig. 6a) and the second lattice direction (i.e., direction b, as shown in Fig. 6a), respectively. The results of microscopic instability (periodicity) and macroscopic instability (ellipticity) are presented in Fig. 6b and c, respectively. In particular, Fig. 6c shows that critical strain to macroscopic instability is smaller than that to microscopic instability.

From numerical instability analyses, it was found that the chiral cells' critical strain to macroscopic instability is smaller than that to microscopic instability. The critical periodicity is $(1, \infty)$ and the critical strain is close to 0.085, which is about three times larger than that of the re-entrant honeycomb. In addition, when the chiral cell is subjected to the critical strain to instability, the large part of structural surface is already in contacts exhibiting a gradual progress of deformation. This infinitely periodic unit-cell simulation results are consistent with the observation from the finite-size specimens in Section 2, where the compressed chiral structure does not show any drastic instability.

5. Analytical model for predicting the instability and auxetic effects

5.1. Re-entrant honeycomb

In addition, we also analytically investigate micro-instability of the re-entrant honeycomb by following the work by Gibson and Ashby (Gibson and Ashby, 2010). Since direction 2 is the critical direction for instability, based on Euler-Bernoulli beam theory, the critical strain for the instability within one RVE under compression in direction 2 was derived as a function of h/l and θ:

$$\varepsilon^{i}_{cr2} = \frac{n^2\pi^2 l^2 cos^2\theta}{24h^2(h/l + sin\theta)}, \tag{3}$$

where, n is the rotational stiffness, depending on the degree of constraint to rotation at the ends of the ribs (Gibson and Ashby, 2010). On the other hand, based on the kinematics constrains of the re-entrant honeycomb deformed under compression in direction 2, the limiting strain for the self-contact between the ribs can be derived as (details were provided in the Appendix **S3**):

$$\varepsilon^{c}_{cr2} = \frac{h/l - 2sin\theta}{2h/l - 2sin\theta}. \tag{4}$$

So, the limiting strain ε^{*}_{cr2} of the honeycomb for the auxetic effects in direction 2 can be determined as:

$$\varepsilon^{*}_{cr2} = min\left(\varepsilon^{c}_{cr2},\ \varepsilon^{i}_{cr2}\right). \tag{5}$$

The Poisson's ratio of re-entrant honeycomb was derived as a function of h/l and θ (Gibson and Ashby, 2010) as,

$$\nu_{21} = \frac{\left(\frac{h}{l} - sin\theta\right)(-sin\theta)}{cos^2\theta}. \tag{6}$$

The FE results and the analytical predictions are compared in Fig. 7a, in which the FE results are marked as circular symbols. The shaded areas represent the design space for the re-entrant honeycomb to preserve auxetic effect under compression. Generally, the FE simulations are consistent with the analytical predictions. The slight differences between the FE and theoretical results are indebted to the assumptions of Euler-Bernoulli beam theory.

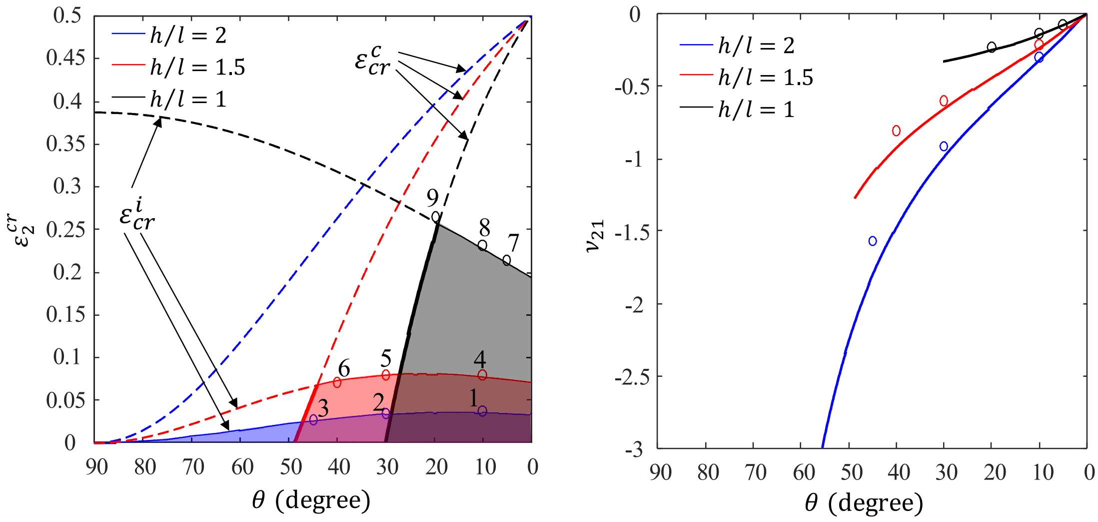

(a)

(b)

Fig. 7. (a) Comparison of the theoretical and FE results of the limiting strain vs. re-entrant angle, and (b) the comparison of the theoretical and FE results of the Poisson's ratio for re-entrant honeycombs for the cases of $l/t = 10$.

Also, the FE and analytical results of the initial Poisson's ratio are shown in Fig. 7b. It can be seen that when h/l increases and/or θ decreases, the Poisson's ratio decreases.

5.2. Chiral cellular solids

For chiral cells, since macroinstability is more critical than microinstability, the self-contact between the ribs can be an approximate criterion for losing auxetic effects. Based on a rigid-rod-rotational spring model (Jiang and Li, 2017a), through kinematic analysis, the critical strain for self-contact of a chiral cell can be derived as (details were provided in the Appendix **S4**),

$$\varepsilon^c_{cr2} = \frac{\sin\left(\frac{\alpha}{2} - \frac{3\alpha+\beta-\pi}{6+2R_{p/a}}\right) - \sin\frac{\alpha}{2}}{\sin\frac{\alpha}{2}}, \tag{7}$$

where $R_{p/a}$ is the internal rotation efficiency which depends on the ratio between the rotational stiffness of the rotational springs K_θ/K_β, in which, as shown in Fig. **S2** (b), K_θ is the rotational stiffness of the rotational spring located at the center of the chiral cell in the rigid-rod-rotational-spring model (Jiang and Li, 2017a) and K_β is the rotational stiffness of the rotational springs connecting the passive ribs. From a systematic parametric study via FE simulations, we find that $R_{p/a}$ is usually larger than 0.45 for all different geometries of chiral cells. Therefore, $R_{p/a} = 0.45$ will be used to predict the upper bounds of the Poisson's ratio for the chiral cellular solids. In addition, based on the rigid-rod rotational spring model, the Poisson's ratio of chiral cellular solids was derived by Jiang and Li (2017a) as,

$$\nu_{21} = \frac{\tan(\alpha/2)}{\tan(\beta/2)} R_{p/a}. \tag{8}$$

6. Design space for preserving auxetic effects under compression

For auxetic material, the Poisson's ratio is an important material property and the value of it is critical to evaluate the mechanical performance. As shown in Section 2, the auxetic effect of cellular solids will disappear after instability and contact between ribs under compression. Therefore, for the purpose of design, it is important to investigate not only the auxetic effect but also the limiting strain under which the auxetic effect is preserved. In this section, the relationship between the Poisson's ratio before the limiting strain and the value of the limiting strain are evaluated, providing a useful parametric design map for both cells.

According to Eqs. (3)–(8), the design spaces for re-entrant honeycombs and the chiral cellular solids can be determined from the plots of the Poisson's ratio vs. overall limiting compressive strain for losing auxetic effects for all possible geometries. For the re-entrant honeycomb, according to Eqs. (3)–(6), the lower bounds of the Poisson's ratio and the limiting strain for all possible geometries are plotted in Fig. 8a as functions of h/l and θ. For the chiral cellular solids, according to Eqs. (7) and (8), the upper bounds of the Poisson's ratio and the limiting strain for all possible geometries are plotted in Fig. 8b as functions of α and β.

For the re-entrant honeycombs, Fig. 8a shows that when θ decreases, and/or h/l increases, the Poisson's ratio will be reduced, indicating a stronger auxetic effect. For example, for the curve of $\theta = 20°$ in Fig. 8a (left), from A to B, h/l increases; and from B to C and beyond, h/l also increases. The point B corresponds to the case of the critical strain for the instability coincides with the limiting strain of self-contact (i.e., $\varepsilon^c_{cr2} = \varepsilon^i_{cr2}$). For the curve of $\frac{h}{l} = 0.9$ in Fig. 8a (right), from A' to B', θ decreases; and from B' to C', θ also decreases. Similarly, the point B' corresponds to the case of the critical strain for the instability coincides with the limiting strain of self-contact (i.e., $\varepsilon^c_{cr2} = \varepsilon^i_{cr2}$). However, the reduction in Poisson's ratio is accompanied by the significant reduction of the limiting strain to lose auxetic effect.

For the chiral cellular solids, Fig. 8b shows that when α increases, and/or β decreases, the Poisson's ratio can be reduced. Although the limiting strain to lose auxeticity will also be reduced to some extend compared with re-entrant honeycombs, the chiral cellular solids can preserve auxetic effect under much large deformation. For example, for the chiral cellular solids, the limiting strain for losing auxetic effects is always larger than ~30% when α is larger than 90° and β is larger than 20°.

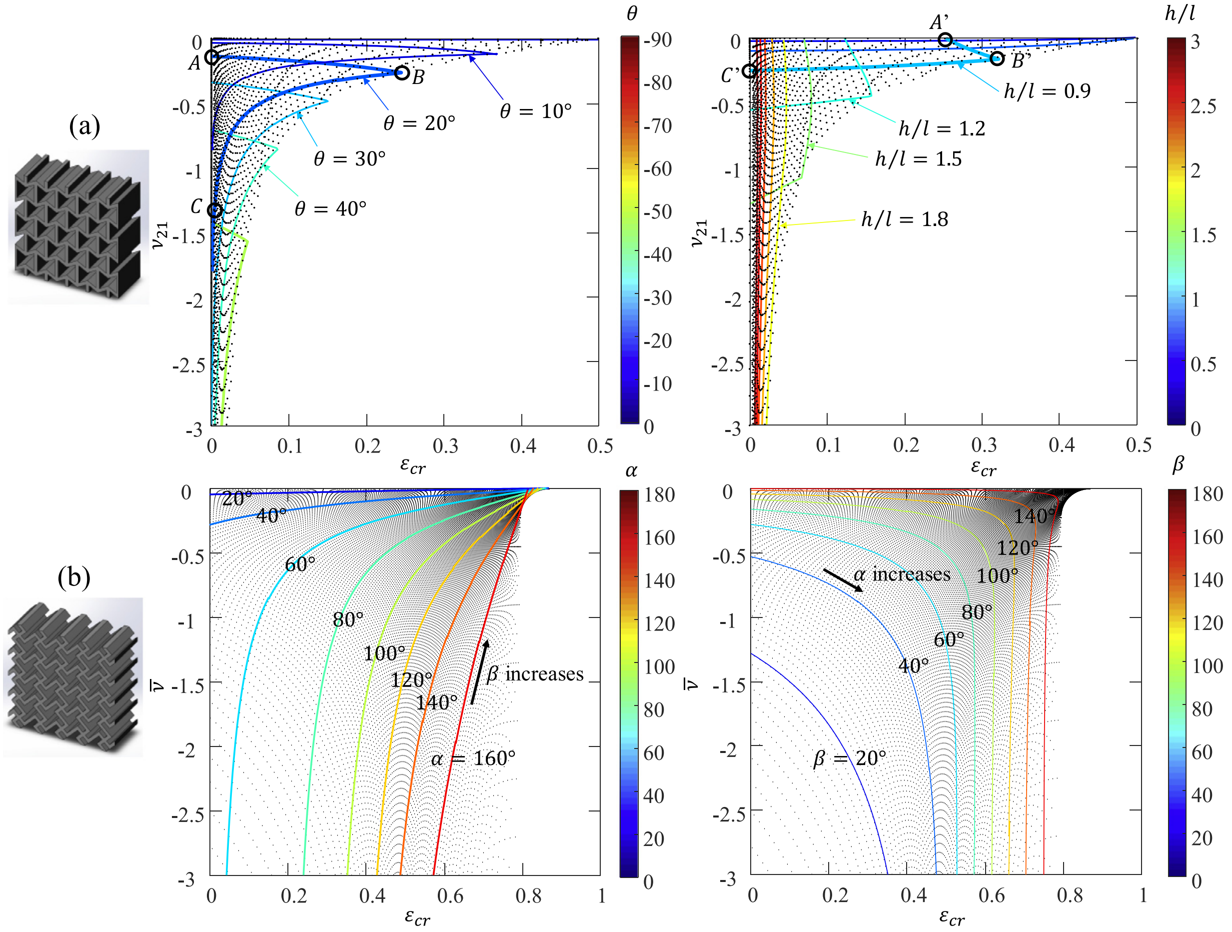

Fig. 8. The design space of Poisson's ratio vs. limiting strain of auxetic effect for all possible geometries of (a) the re-entrant honeycombs and (b) the 'missing-rib' type of chiral cellular solids.

8. Conclusions

Due to the instability and contact between the ribs, auxetic open cell cellular solids may lose auxeticity beyond certain compressive strain. We have explored the limiting strains for preserving auxetic effects for auxetic open cell materials of two types: re-entrant honeycomb and the 'missing-rib' type chiral cellular solids. Mechanical experiments of the 3D printed specimens show that re-entrant honeycomb subjected to compression suffers instability before hardening while the chiral specimen under compression does not exhibit drastic instability before rib contact. A series of FE simulations using a unit-cell model with periodic boundary conditions confirm the instability behavior of the finite-size specimens of those two type of auxetic structures

Moreover, we have quantified the relation between the Poisson's ratio and the limiting strain for losing auxetic effects for both re-entrant honeycombs and chiral cellular solids. For both types of lattices, the auxetic effects and the limiting compressive strain for auxetic effects are mutually exclusive, i.e., if the goal is to achieve a more negative Poisson's ratio (a stronger auxetic effects), the sacrifice needs to be made on the limiting strain for preserving this auxetic effects. For all the possible geometries, the re-entrant honeycombs can only preserve strong auxetic effects under very small overall compressive strain ($< \sim 3$ and 4%), beyond which auxetic effects will be lost. However, due to the chirality-induced rotation, the chiral cellular solids can preserve auxetic effects under much larger compressive strain ($> \sim 10$–30%). These results provide useful guideline for designing auxetic materials to sustain auxetic effects under larger deformation.

Here are some physical insights on the observation that the limiting strain for observing auxeticity in the re-entrant honeycomb is lower than that in the chiral cells: for the re-entrant honeycombs, there are two axes of in-plane mirror symmetry; however, for the chiral cells, there is no axis of in-plane mirror symmetry. For the re-entrant honeycombs, the auxetic effects is due to the symmetry; while for the chiral cells, the auxetic effects is due to chirality induced rotation. Physically, the nature of the instability is to break symmetry, therefore, after instability, the re-entrant honeycombs will lose auxetic effects. While the chiral cells have no symmetry to break, so the auxetic effects can be preserved for larger deformation.

Acknowledgements

Jiang and Li acknowledge the supports from National Science Foundation of the United States (NSF) through grants CMMI-1554468 (CAREER). Rudra and Shim acknowledge the supports from NSF through Grant CMMI-1649111 and UB Center for Computational Research.

Supplementary material

Supplementary material associated with this article can be found, in the online version, at doi:10.1016/j.ijsolstr.2018.11.035.

References

Arruebo, M., 2012. Drug delivery from structured porous inorganic materials. Wire. Nanomed. Nanobi. 4 (1), 16–30.

Babaee, S., Shim, J., Weaver, J.C., Chen, E.R., Patel, N., Bertoldi, K., 2013. 3D soft metamaterials with negative poisson's ratio. Adv. Mater. 25 (36), 5044–5049.

Bertoldi, K., Boyce, M.C., 2008. Mechanically triggered transformations of phononic band gaps in periodic elastomeric structures. Phys. Rev. B. 77 (5), 052105.

Bertoldi, K., Reis, P.M., Willshaw, S., Mullin, T., 2010. Negative poisson's ratio behavior induced by an elastic instability. Adv. Mater. 22 (3), 361–366.

Chan, N., Evans, K.E., 1998. Indentation resilience of conventional and auxetic foams. J. Cell. Plast. 34 (3), 231–260.

Chen, C.P., Lakes, R.S., 1989. Dynamic wave-dispersion and loss properties of conventional and negative poissons ratio polymeric cellular materials. Cell. Polym. 8 (5), 343–359.

Dolla, W.J.S., Fricke, B.A., Becker, B.R., 2007. Auxetic drug-eluting stent design. In: Proceedings of the Frontiers in Biomedical Devices Conference., pp. 11–12.

Evans, K.E., Alderson, A., 2000. Auxetic materials: functional materials and structures from lateral thinking!. Adv. Mater. 12 (9), 617–628.

Fozdar, D.Y., Soman, P., Lee, J.W., Han, L.H., Chen, S.C., 2011. Three-dimensional polymer constructs exhibiting a tunable negative poisson's ratio. Adv. Funct. Mater. 21 (14), 2712–2720.

Gibson, L.J., Ashby, M.F., 2010. Cellular Solids: Structure and Properties, 2nd ed Cambridge Univ. Press, Cambridge, USA.

Geymonat, G., Müller, S., Triantafyllidis, N., 1993. Homogenization of nonlinearly elastic materials, microscopic bifurcation and macroscopic loss of rank-one convexity. Arch. Ration. Mech. Anal. 122 (3), 231–290.

Grima, J.N., Mizzi, L., Azzopardi, K.M., Gatt, R., 2016. Auxetic perforated mechanical metamaterials with randomly oriented cuts. Adv. Mater. 28 (2), 385–389.

Guiducci, L., Fratzl, P., Bréchet, Y.J., Dunlop, J.W., 2014. Pressurized honeycombs as soft-actuators: a theoretical study. J. R. Soc. Interface 11 (98), 20140458.

Haghpanah, B., Papadopoulos, J., Mousanezhad, D., Nayeb-Hashemi, H., Vaziri, A., 2014. Buckling of regular, chiral and hierarchical honeycombs under a general macroscopic stress state. Proc. R. Soc. a 470 (2167), 20130856.

Ji, W., Waas, A.M., 2007. Global and local buckling of a sandwich beam. ASCE J. Eng. Mech. 133 (2), 230–237.

Jiang, Y., Li, Y., 2017a. 3D printed chiral cellular solids with amplified auxetic effects due to elevated internal rotation. Adv. Eng. Mater. 19 (2), 1600609.

Jiang, Y., Li, Y.N., 2017b. Novel 3D-printed hybrid auxetic mechanical metamaterial with chirality-induced sequential cell opening mechanisms. Adv. Eng. Mater. (Front Cover) 20 (2), 1700744.

Jiang, Y., Li, Y., 2018. 3D Printed auxetic mechanical metamaterial with chiral cells and re-entrant cores. Scientif Rep. 8 (1), 2397.

Lakes, R., 1987. Foam structures with a negative poisson's ratio. Science 235 (4792), 1038–1040.

Lakes, R.S., Elms, K., 1993. Indentability of conventional and negative poisson's ratio foams. J. Compos. Mater. 27 (12), 1193–1202.

Prall, D., Lakes, R.S., 1997. Properties of a chiral honeycomb with a poisson's ratio of -1. Int. J. Mech. Sci. 39 (3), 305–314.

Scarpa, F., Dallocchio, F., Ruzzene, M., 2003. Identification of acoustic properties of auxetic foams. P. Soc. Photo Opt. Ins. 5052, 468–474.

Shim, J., Shan, S., Kosmrlj, A., Kang, S.H., Chen, E.R., Weaver, J.C., Bertoldi, K., 2013. Harnessing instabilities for design of soft reconfigurable auxetic/chiral materials. Soft Matter 9 (34), 8198–8202.

Sigmund, O., Torquato, S., 1997. Design of materials with extreme thermal expansion using a three-phase topology optimization method. J. Mech. Phys. Solid. 45 (6), 1037–1067.

Smith, C.W., Grima, J.N., Evans, K.E., 2000. A novel mechanism for generating auxetic behaviour in reticulated foams: missing rib foam model. Acta. Mater. 48 (17), 4349–4356.

Smith, W.A., 1991. Optimizing electromechanical coupling in piezocomposites using polymers with negative poisson's ratio. In: Proceedings IEEE 1991 Ultrasonics Symposium, December, 1991. IEEE, pp. 661–666.

Tang, Y.C., Lin, G.J., Han, L., Qiu, S.G., Yang, S., Yin, J., 2015. Design of hierarchically cut hinges for highly stretchable and reconfigurable metamaterials with enhanced strength. Adv. Mater. 27 (44), 7181–7190.

Tee, K.F., Spadoni, A., Scarpa, F., Ruzzene, M., 2010. Wave propagation in auxetic tetrachiral honeycombs. J. Vib. Acoust. 132 (3), 031007.

Triantafyllidis, N., Maker, B.N., 1985. On the comparison between microscopic and macroscopic instability mechanisms in a class of fiber-reinforced composites. J. Appl. Mech. 52 (4), 794–800.

Wang, F., Sigmund, O., Jensen, J.S., 2014a. Design of materials with prescribed nonlinear properties. J. Mech. Phys. Solid 69, 156–174.

Wang, P., Casadei, F., Shan, S., Weaver, J.C., Bertoldi, K., 2014b. Harnessing buckling to design tunable locally resonant acoustic metamaterials. Phys. Rev. Lett. 113 (1), 014301.

Waas, A.M., Babcock Jr., C.D., Knauss, W.G., 1990. A mechanical model for elastic fiber microbuckling. ASME. J. Appl. Mech. 57 (1), 138–149.

Wu, G.X., Cho, Y., Choi, I.S., Ge, D.T., Li, J., Han, H.N., Lubensky, T., Yang, S., 2015. Directing the deformation paths of soft metamaterials with prescribed asymmetric units. Adv. Mater. 27 (17), 2747–2752.

Wang, P., Casadei, F., Shan, S., Weaver, J.C., Bertoldi, K., 2014c. Harnessing buckling to design tunable locally resonant acoustic metamaterials. Phys. Rev. Lett. 113 (1), 014301.

Zhang, Q., Yan, D., Zhang, K., Hu, G., 2015. Pattern transformation of heat-shrinkable polymer by three-dimensional (3D) printing technique. Sci. Rep. 5, 8936.

Appendix

S1. Microscopic instability (Periodicity analysis)

Microscopic (local) buckling modes may alter the initial periodicity of the solid. To explore microscopic instability of enlarged unit cells spanned by lattice vectors $m_1\mathbf{a}_1$ and $m_2\mathbf{a}_2$ (positive integer m_i and primitive lattice vector $\mathbf{a}_i$ for $i = 1,2$), we consider a single primitive unit cell and apply Bloch-periodic conditions (Geymonat et al., 1993; Bertoldi and Boyce, 2008):

$$\bar{\mathbf{u}}(\mathbf{x} + \mathbf{r}) = \bar{\mathbf{u}}(\mathbf{x})\, \mathrm{e}^{i\mathbf{k}\cdot\mathbf{r}} \tag{A1}$$

where, the Bloch wavevector $\mathbf{k} = \mathbf{b}_1/m_1 + \mathbf{b}_2/m_2$, and $\mathbf{b}_i$ (or $i = 1,2$) is the primitive reciprocal vector. To work with the complex-valued relations of the Bloch-periodic conditions in ABAQUS, all fields are split into real and imaginary parts. In this way, the equilibrium equations are divided into two sets of uncoupled equations for the real and imaginary parts (Aberg and Gudmundson, 1997; Shim et al., 2015). For a given enlarged unit cell defined by m_1 and m_2, the microscopic stability is investigated by identifying the applied load at which the smallest eigenfrequency associated to a non-trivial eigenmode become zero (Bathe, 1996). Then, the onset of instability for the infinite periodic structure is defined as the minimum critical strain on all the considered enlarged unit cells defined by m_1 and m_2. Here, we typically investigate the stability of 25 enlarged primitive units by choosing $m_1 = 1, \dots, 5$ and $m_2 = 1, \dots, 5$.

S2 Macroscopic instability (Ellipticity analysis)

Macroscopic instability corresponds to loss of ellipticity at the macroscopic scale (Geymonat et al., 1993), and it can be investigated by detecting when the homogenized mixed elasticity tensor $\widetilde{\mathbb{L}}$ violates the positive definite conditions (Marsden and Hughes, 1983):

$$(\mathbf{m}\otimes\mathbf{N}):\tilde{\mathbb{L}}:(\mathbf{m}\otimes\mathbf{N}) > 0 \quad , \qquad m_i N_J m_k N_L \mathcal{L}_{iJkL} > 0 \quad , \tag{A2}$$

for all $\mathbf{m}\otimes\mathbf{N} \neq \mathbf{0}$, where $\mathbf{m}$ and $\mathbf{N}$ are unit vectors defined in the deformed and the undeformed configurations, respectively. Note that $\tilde{\blacksquare}$ denotes homogenized quantity. In this study, a single primitive unit cell with the spatially periodic boundary conditions (Eq.A1) is subjected to four independent linear perturbations of the macroscopic deformation gradient $\tilde{\mathbf{F}}$. Then, the components of $\tilde{\mathbb{L}}$ are identified by calculating the corresponding averaged first Piola-Kirchhoff stress components $\tilde{\mathbf{P}}$ from $\tilde{\mathbf{P}} = \mathbb{L}:\tilde{\mathbf{F}}$ (Bertoldi and Boyce, 2008, Shim et al., 2015). Eventually, we check the loss of ellipticity condition (Eq.A2) by changing $\mathbf{m}$ and $\mathbf{N}$ separately explored at every $\pi/360$ radian increment.

S3. Self-contact strain for re-entrant honeycomb

The schematics of the self-contact mechanism of re-entrant honeycomb under uni-axial compression in direction D2 is shown in Fig.S1.

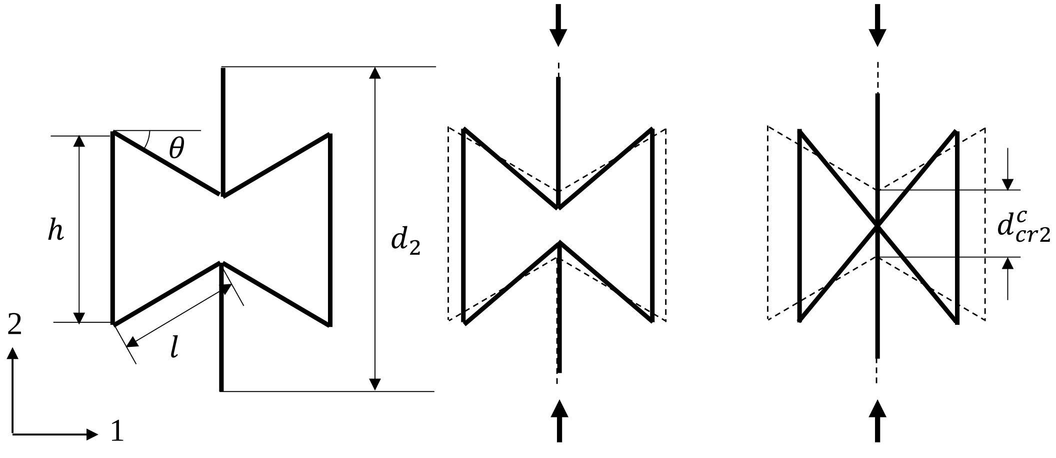

(a) (b) (c)

Figure S1 The schematics of the self-contact mechanism of re-entrant cell under uni-axial compression along direction 2.

The critical displacement d_{cr2}^{c} for self-contact under compression along direction 2 is shownin Fig.S1c and can be expressed as

$$d_{cr2}^{c} = h - 2lsin\theta \ . \tag{A.3}$$

The original length of the RVE along direction 2 is

$$d_2 = 2h - 2lsin\theta \ . \tag{A.4}$$

Therefore, the critical strain for self-contact of the re-entrant cell along direction 2 can be derived as,

$$\varepsilon_{cr2}^{c} = \frac{d_{cr2}^{c}}{d_2} = \frac{h-2lsin\theta}{2h-2lsin\theta} = \frac{h/l-2sin\theta}{2h/l-2sin\theta} \ . \tag{A.5}$$

S4. Self-contact strain for chiral cell

The schematics of the self-contact mechanism of a chiral cell under un-axial compression in shown in Fig.S2.

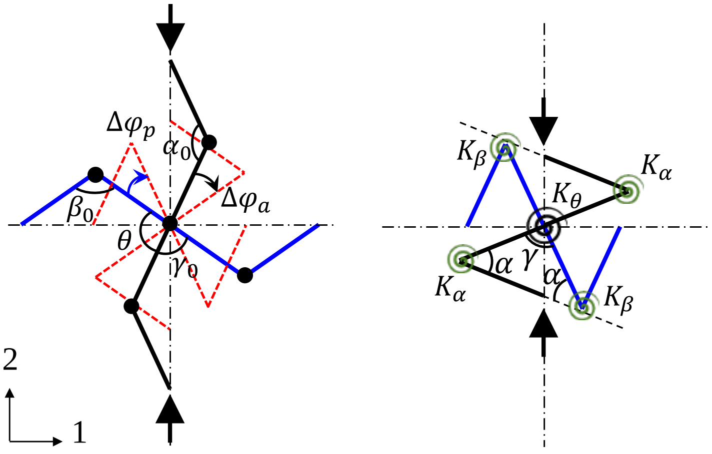

(a)

(b)

Figure S2 The schematics of the self-contact mechanism of a chiral cell under uni-axial compression along direction 2.

The initial length of the RVE in direction 2 can be represented as,

$$d_{20} = 4a\sin(\alpha_0/2), \tag{A.6}$$

where a is the length of the ribs of the chiral cellular, α_0 is the initial angle between the active ribs along direction 2. When self-contact occurs, the length of the RVE in direction 2 can be represented as,

$$d_2 = 4a\sin(\alpha/2), \tag{A.7}$$

where α is the angle between the active ribs along direction 2 when self-contact occurs. α can be derived as,

$$\alpha = \alpha_0 - 2\Delta\varphi_a, \tag{A.8}$$

where $\Delta\varphi_a$ is the rotation angle of the active ribs under deformation as shown in Fig. S2a.

Therefore, the critical strain for self-contact of a chiral cell along direction 2 can be derived as,

$$\varepsilon_{cr2}^{c} = \frac{d_{20}-d_2}{d_{20}} = \frac{sin\left(\frac{\alpha_0}{2}-\Delta\varphi_a\right)-sin\frac{\alpha_0}{2}}{sin\frac{\alpha_0}{2}}\,. \tag{A.9}$$

$\Delta\varphi_a$ can be found from the relation between γ_0 and γ, which are the angles between the active ribs and passive ribs before deformation and after self-contact, respectively.

From the kinematics, γ_0 can be expressed as,

$$\gamma_0 = \frac{\pi}{2} - \frac{\alpha_0}{2} + \frac{\beta_0}{2}\,. \tag{A.10}$$

Then, γ is expressed as,

$$\gamma = \gamma_0 + \Delta\varphi_a - \Delta\varphi_p\ , \tag{A.11}$$

where $\Delta\varphi_p$ is the rotation angle of the passive ribs, which can be represented as $R_{p/a}\Delta\varphi_a$. Thus, Eq.A11 becomes,

$$\gamma = \gamma_0 + \left(1 - R_{p/a}\right)\Delta\varphi_a = \frac{\pi}{2} - \frac{\alpha_0}{2} + \frac{\beta_0}{2} + \left(1 - R_{p/a}\right)\Delta\varphi_a. \qquad \text{(A.12)}$$

When self-contact occurs, the following equation holds, as shown in Fig.S2b

$$\gamma + 2\alpha = \pi. \qquad \text{(A.13)}$$

By combining Eqn.A8, A12 and A13, $\Delta\varphi_a$ can be derived as:

$$\Delta\varphi_a = \frac{3\alpha_0 + \beta_0 - \pi}{6 + 2R_{p/a}}. \qquad \text{(A.14)}$$

Thus, the limiting strain for the auxetic effects for the auxetic chiral cellular solid can be derived as:

$$\varepsilon_{cr2}^{c} = \frac{sin\left(\frac{\alpha_0}{2} - \mathit{\Delta}\varphi_a\right) - sin\frac{\alpha_0}{2}}{sin\frac{\alpha_0}{2}}, \qquad \text{(A15)}$$

where, $\mathit{\Delta}\varphi_a = \frac{3\alpha_0 + \beta_0 - \pi}{6 + 2R_{p/a}}$.